# Dynamics and statistics of wave-particle interactions in a confined geometry

Tristan Gilet[1, *]

[1]*Microfluidics Lab, GRASP,*
*Department of Aerospace and Mechanics,*
*University of Liège, B-4000 Liège, Belgium*

A walker is a droplet bouncing on a liquid surface and propelled by the waves that it generates. This macroscopic wave-particle association exhibits behaviors reminiscent of quantum particles. This article presents a toy model of the coupling between a particle and a confined standing wave. The resulting 2D iterated map captures many features of the walker dynamics observed in different configurations of confinement. These features include the time decomposition of the chaotic trajectory in quantized eigenstates, and the particle statistics being shaped by the wave. It shows that deterministic wave-particle coupling expressed in its simplest form can account for some quantum-like behaviors.
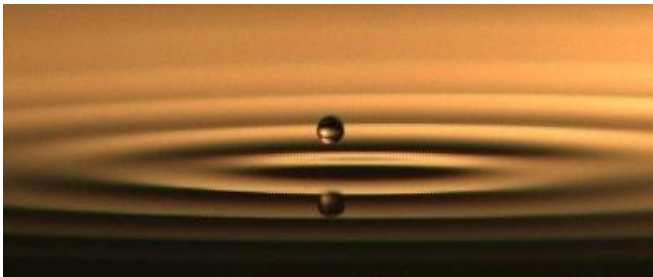
## I. INTRODUCTION



FIG. 1. (Color online) Macroscopic wave-particle coupling. A walker is a millimetric oil droplet that bounces onto a vertically vibrated liquid pool. The Faraday waves generated by the droplet impacts propel this latter horizontally.

In recent experiments, Y. Couder and co-workers have investigated the coupling between a classical particle and a wave. The particle is a millimetric droplet that bounces at the surface of a vertically vibrated liquid bath (Fig.1) [1–3]. The droplet creates a circular capillary wave every time it impacts the surface. As this wave travels away, it excites standing Faraday waves in its wake. The damping time of Faraday waves increases as the amplitude of the forcing vibration approaches the Faraday instability threshold. Memory $M$ is defined as this damping time divided by the time between successive rebounds. Consequently, the droplet impacts on a liquid surface corrugated by the Faraday waves resulting from its last $M$ impacts. When $M \gg 1$, the wavy surface then gives a small horizontal impulse to the droplet, which starts walking on the liquid surface. The Faraday wave is only sustained by the local excitation of the droplet, which in turn moves horizontally only because of the wave. There-

* Tristan.Gilet@ulg.ac.be

fore, this system, now referred as a walker, exhibits a strong coupling between a wave and a particle.

At high memory (typically $M \gtrsim 30$), walkers show properties that are highly reminiscent of quantum particles in many different contexts (incl. diffraction and double-slit interferences [4], tunneling [5], Zeeman effect [6]). A recent review summarizes our current understanding of this analogy after a decade of investigations [7]. Of more interest for the present work, individual walkers have been experimentally observed to follow quantized orbital trajectories in three different contexts that all involve some confinement:

(i) in a rotating frame (Coriolis force) [8–10],

(ii) in a central force field (harmonic potential) [11],

(iii) in a confined geometry (potential well) [12, 13].

Several properties are invariantly seen in experiments (i–iii). For example, in (i) and (ii), it has been shown that at relatively low memory ($M \sim 10$), the walker follows stable regular orbits which spatial extension varies continuously with the control parameter [rotation rate in (i), potential width in (ii)] as in classical mechanics. It is also expected that in (iii) these orbital radii would vary continuously with cavity size. At higher memory ($M \sim 50$) the walker often revisits regions where the waves from previous visits are still present, and the trajectory usually becomes chaotic. More exactly, it follows unstable regular orbits assimilated to eigenstates. The walker stays in each of them for a certain time before it switches to another (Fig.10 in [9], Fig.6 in [11]). These orbital eigenstates are quantized and now insensitive to the control parameters. Their spatial extension is always an integer multiple of half the Faraday wavelength $2\pi/k_F$, which can then be seen as the analog of the de Broglie wavelength [8]. The probability to find the walker in a given state is proportional to the relative amount of time spent in this state. In addition, in the confined geometry (iii), it was shown that the Probability Distribution Function (PDF) of the walker position is directly shaped by the resonant eigenmodes of the cavity. A realistic model of

walker dynamics has recently been developed by A. Oza *et al.* [3, 10]. The resulting integro-differential equation for the droplet horizontal position accurately reproduces the experimental results obtained for (i). Nevertheless, the evident similarity of walker behavior in different configurations (ii–iii) suggests that this dynamics is shared by a much larger set of wave-particle systems.

In section II, a general framework for the description of wave-particle interaction with geometry confinement is first established. The model is then particularized (section III) and simplified to the point where both wave and particle dynamics are each represented by a single scalar recurrence relation. The iterated map involves a wave function $\Psi(x)$ which prescribes the shape of the standing wave. Fixed points and stability are then calculated analytically. In section IV, numerical simulations are performed for seven particular functions $\Psi(x)$. The transition to chaos is analyzed in section V, as well as the statistical behavior in the chaotic regime. Finally, the intermittent switch between unstable eigenstates is discussed in section VI.

## II. WAVE-PARTICLE COUPLING IN A CONFINED GEOMETRY

This paper first presents a model of a walker confined to a domain $\Omega$. This model is intended to represent the geometry confinement of experiment (iii), though most of its features are thought to be generic of any confinement. The standing Faraday wave field $h_n(\mathbf{x})$ resulting from the $n$ first impacts is decomposed in the discrete basis of eigenmodes $\Psi_k(\mathbf{x})$ of the domain.

$$h_n(\mathbf{x}) = \sum_k W_{k,n}\Psi_k(\mathbf{x}), \quad W_{k,n} = \int_\Omega h_n(\mathbf{x})\Psi_k^*(\mathbf{x})d\Omega$$

(1)

where $\Psi_k^*$ is the conjugate of $\Psi_k$. These eigenmodes are orthonormal on $\Omega$ and satisfy $\mathbf{n}\cdot\nabla\Psi_k = 0$ at the boundary $\partial\Omega$ of normal vector $\mathbf{n}$. Traveling capillary waves are neglected since they spread their initial energy in 2D and they are not energized by the vertical forcing [1], so they do not likely affect the long term statistics. Only when the particle comes close to the boundary could these capillary waves significantly modify the local trajectory. But this effect would then be localized in space and time, so it is not expected to strongly affect the particle statistics.

At rebound $n$, the walker impacts the liquid bath at position $\mathbf{x}_n$ and creates a crater of shape $z = f(y)$ in the wave-field, where $\mathbf{y} = \mathbf{r} - \mathbf{x}_n$ and $y = ||\mathbf{y}||$. This crater can be decomposed in the basis of $\Psi_k$:

$$f(y) = \sum_k c_k\Psi_k(\mathbf{r}), \quad c_k = \int_\Omega f(y)\Psi_k^*(\mathbf{r})d\Omega$$

(2)

The crater is localized in a region of radius $R$ about the impact point, so

$$c_k \simeq \int_0^{2\pi} d\theta \int_0^R f(y)ydy\,\Psi_k^*(\mathbf{x}_n + \mathbf{y})$$

(3)

If $R$ is much smaller than the characteristic wavelength of $\Psi_k$, then $\Psi_k^*(\mathbf{x}_n + \mathbf{y}) \simeq \Psi_k^*(\mathbf{x}_n) + \mathbf{y}\cdot\nabla\Psi_k^*]_{\mathbf{x}_n}$ and therefore

$$c_k \simeq \Psi_k^*(\mathbf{x}_n)\int_0^{2\pi}d\theta\int_0^R f(y)ydy$$
$$+ \nabla\Psi_k^*]_{\mathbf{x}_n}\cdot\int_0^{2\pi}d\theta\int_0^R y\mathbf{y}f(y)dy$$

(4)

The second term is zero by symmetry, so $c_k \simeq A\Psi_k^*(\mathbf{x}_n)$, where the constant

$$A = \int_0^{2\pi}d\theta\int_0^R f(y)ydy \simeq \int_\Omega f(y)dy$$

(5)

corresponds to the volume of liquid displaced by one impact. The crater is finally represented by

$$f(y) = A\sum_k \Psi_k^*(\mathbf{x}_n)\Psi_k(\mathbf{r}) = A\delta(\mathbf{r} - \mathbf{x}_n)$$

(6)

The crater is thus assumed equivalent to a delta function at the impact point, weighted by the volume of liquid displaced. The contribution of the impact to each wave eigenmode $A\Psi_k^*(\mathbf{x}_n)$ strongly depends on the particle position. We now normalize the wave field $h_n(\mathbf{x})$ by $A$.

For every forcing conditions, a damping factor $\mu_k \in [0,1]$ can be associated to each $\Psi_k(\mathbf{x})$. It is defined as the amplitude of mode $k$ right before impact $n+1$, divided by its amplitude right after impact $n$. It can be estimated by spectral methods [14] and by definition $\mu_k^{M_k} = e^{-1}$, where $M_k$ is the memory associated to mode $k$. The Faraday threshold instability corresponds to $\max(\mu_k) = 1$. The amplitude of each mode $W_{k,N}$ then satisfies the recurrence relation

$$W_{k,n+1} = \mu_k\left(\Psi_k^*(\mathbf{x}_n) + W_{k,n}\right)$$

(7)

At each impact, the particle is shifted proportionally to the gradient of the wave field at the impact position:

$$\mathbf{x}_{n+1} = \mathbf{x}_n - C\sum_k W_{k,n}\,\nabla\Psi_k]_{\mathbf{x}_n}$$

(8)

where $C > 0$ is a constant that represents the strength of the wave-particle coupling. This hypothesis is different from previous models (e.g. [13]) where the force (instead of the velocity) is proportional to the wave slope. Equations 7 and 8 form an iterated map that describes the evolution of the walker in configuration (iii). Nevertheless, this modal approach is also likely relevant to configurations (i) and (ii) where confinement does not originate from physical boundaries. Especially in (ii) [11], Graf's addition theorem states that the wave field can always be decomposed in cylindrical harmonics centered on the force field. Each harmonic is then excited according to the walker position, similarly to (7).

## III. A TOY MODEL FOR THE WAVE-PARTICLE COUPLING

A detailed analysis of this map (7–8) and comparison to the experiments in (iii) is the object of another publication. This work aims at reaching the simplest model that still captures the features of confined wave-particle coupling observed experimentally. We thus now consider the map where only one direction $x$ and one mode $\Psi(x) \in \mathbb{R}$ of damping $\mu$ are kept:

$$\begin{cases} w_{n+1} = \mu\left[w_n + \Psi(x_n)\right] \\ x_{n+1} = x_n - Cw_n\Psi'(x_n) \end{cases} \quad (9)$$

The map allows for two families of fixed points:

$$(x_a, w_a), \text{ where } \Psi(x_a) = 0, w_a = 0 \quad (10)$$

and

$$(x_b, w_b), \text{ where } \Psi'(x_b) = 0, w_b = \frac{\mu}{1-\mu}\Psi(x_b) \quad (11)$$

For convenience, we denote $\Psi_a = \Psi(x_a)$, $\Psi'_b = \Psi'(x_b)$ and so on.

Fixed points of the first family correspond to a position where an impact does not excite any wave. Their linear stability is assessed by analyzing the growth rate of a small perturbation $(\tilde{x}, \tilde{w}) = (x - x_a, w - w_a)$. The resulting linear map

$$\begin{cases} \tilde{w}_{n+1} = \mu\tilde{w}_n + \mu\Psi'_a\tilde{x}_n \\ \tilde{x}_{n+1} = \tilde{x}_n - C\Psi'_a\tilde{w}_n \end{cases} \quad (12)$$

has a characteristic equation

$$z^2 - (\mu+1)z + \mu\left[1 + C\Psi'^2_a\right] = 0 \quad (13)$$

that is solved by substituting $z = \rho e^{i\theta}$:

$$\begin{cases} \cos\theta = \frac{\rho(1+\mu)}{\rho^2 + \mu\left(1 + C\Psi'^2_a\right)} \\ \sin\theta\left[\rho^2 - \mu\left(1 + C\Psi'^2_a\right)\right] = 0 \end{cases} \quad (14)$$

Each fixed point $x_a$ gets marginally stable ($\rho = 1$) for a specific damping $\mu = \mu_a$. When the eigenvalues $z$ of the linear map are real ($\theta = 0$), imposing $\rho = 1$ yields $\mu_a = 0$. It is also straightforward to show that when $\theta = 0$, $\rho \in [0, 1]$ for every $\mu \in [0, 1]$ so real eigenvalues always correspond to stable fixed points. If $\theta \neq 0$ (complex conjugate eigenvalues) then $\rho^2 = \mu\left(1 + C\Psi'^2_a\right)$ so the stability condition $\rho \leq 1$ becomes

$$\mu < \mu_a = \frac{1}{1 + C\Psi'^2_a} \in ]0, 1] \quad (15)$$

Eigenvalues are complex when

$$\mu > \mu_c = 1 + 2C\Psi'^2_a - \sqrt{(1 + 2C\Psi'^2_a)^2 - 1} \quad (16)$$

Since $\mu_c < \mu_a$, the bifurcation in $\mu = \mu_a$ is a Neimark-Sacker bifurcation (discrete equivalent of the Hopf bifurcation). It is shown numerically that this bifurcation is supercritical. It gives rise to a stable limit cycle centered on $(x_a, w_a)$ when $\mu > \mu_a$.

The linear map for the perturbations $(\tilde{x}, \tilde{w}) = (x - x_b, w - w_b)$ about fixed points of the second family is:

$$\begin{cases} \tilde{w}_{n+1} = \mu\tilde{w}_n \\ \tilde{x}_{n+1} = \left[1 - \frac{\mu C}{1-\mu}\Psi_b\Psi''_b\right]\tilde{x}_n \end{cases} \quad (17)$$

The manifold along the $w$-direction is always stable, as $\mu \in ]0, 1[$. The $x$-direction is stable when

$$z = 1 - \frac{\mu C}{1-\mu}\Psi_b\Psi''_b \in ]-1, 1[ \quad (18)$$

If $\Psi_b\Psi''_b < 0$, this $x$-manifold is unstable for all $\mu \in ]0, 1[$ and the fixed point is a saddle. If $\Psi_b\Psi''_b > 0$, the fixed point is stable when

$$\mu < \mu_b = \frac{1}{1 + \frac{C\Psi_b\Psi''_b}{2}} \quad (19)$$

For $\mu > \mu_b$, the fixed point is a saddle again.

The behavior of this simplified iterated map (9) is very similar to the radial component of walker trajectory in experiments (i–iii), especially when the wave function $\Psi(x)$ is considered equivalent to $J_0(k_F r)$, where $r$ is the radial position on the orbit and $k_F$ the Faraday wavelength. The fixed points of the map are then equivalent to circular orbits in the experiments. In configurations (i–ii) at intermediate memory $M$ (i.e. small $\mu$), stable circular orbits are indeed observed in $r_a$ with $J_0(k_F r_a) = 0$. The stable orbit reported in configuration (iii) [12] also approximately corresponds to a node of the axisymmetric Faraday wave pattern right above threshold. At these locations, the walker does not generate any radial velocity component so the trajectory remains circular. At higher memory, these orbits destabilize and start wobbling and drifting. In (i) it was shown that orbits of larger radius $r_a$, i.e. smaller $J'_0(k_F r_a)$, destabilize at higher $M$, which is consistent with the fact that fixed points of smaller $|\Psi'_a|$ destabilize at higher $\mu$. The analytical model of (i) [15] shows that wobbling originates from a Hopf bifurcation and is then associated to a pair of complex eigenvalues. The same model [10] reveals the presence of unstable orbits in $r_b$ with $J'_0(k_F r_b) = 0$, again analog here to the second family of fixed points. These orbits have always real eigenvalues, some positive and some negative, so they behave as saddles. The simplified iterated map thus captures well the existence and stability of circular orbits in all three configurations of confined walker trajectories.

## IV. TEST FUNCTIONS AND NUMERICAL RESULTS

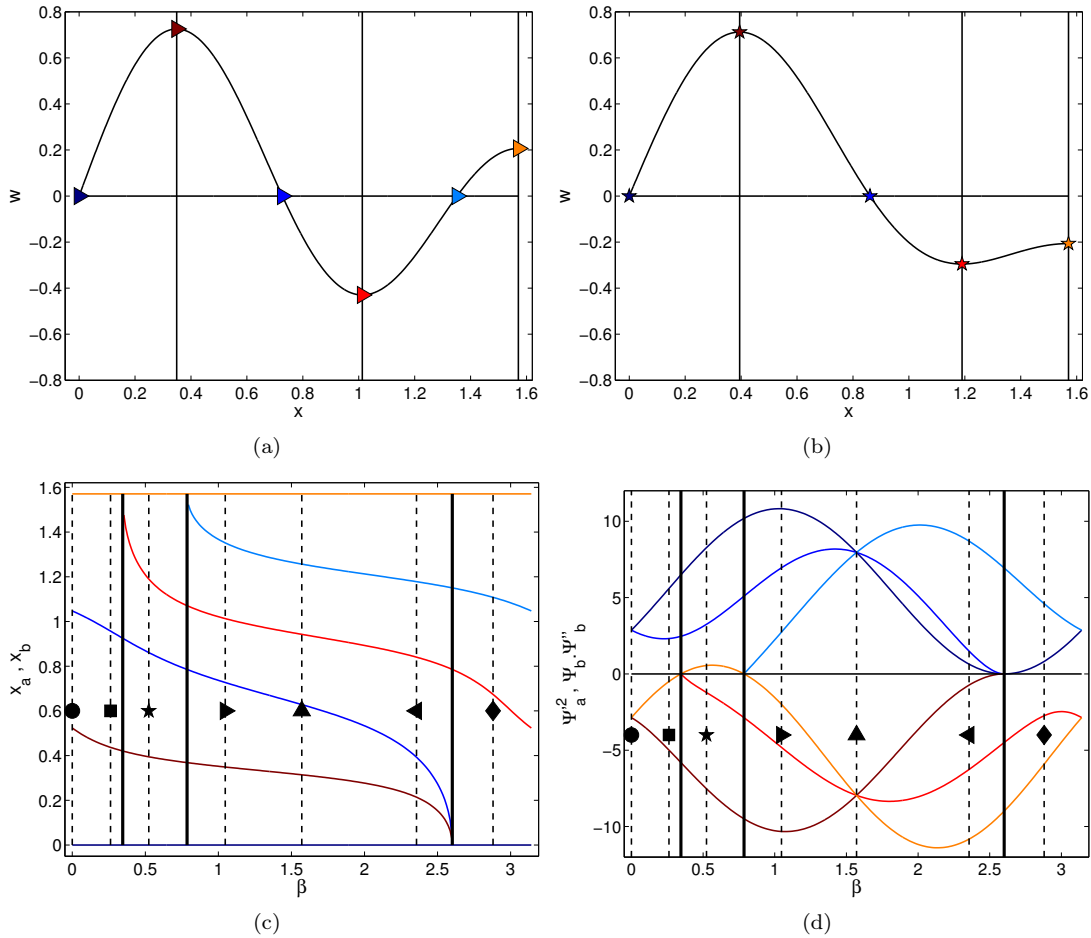In the following, the map dynamics is further investigated numerically for a specific set of functions $\Psi$ and a

FIG. 2. (Color online) Family of test functions $\Psi(x,\beta)$. (a-b) Nullclines and fixed points for (a) $\beta = \pi/3$ and (b) $\beta = \pi/6$. (c) Position of the fixed points $x_a$ (blue tones, in $w = 0$) and $x_b$ (red tones, extrema of $\Psi(x,\beta)$) as functions of the shape parameter $\beta$. (d) Parameters $\Psi_a'^2$ (blue tones – three upper curves) and $\Psi_b\Psi_b''$ (red tones – three lower curves) as functions of $\beta$. In (c-d), the dashed lines indicate the seven values of $\beta$ selected for the numerical analysis. Each of them corresponds to a different symbol: ($\bullet$) $\beta = 0$, ($\blacksquare$) $\beta = \pi/12$, ($\star$) $\beta = \pi/6$, ($\blacktriangleright$) $\beta = \pi/3$, ($\blacktriangle$) $\beta = \pi/2$, ($\blacktriangleleft$) $\beta = 3\pi/4$, and ($\blacklozenge$) $\beta = 11\pi/12$. Colors correspond to different fixed points (Blue tones are always used for $x_a$ while red tones refer to $x_b$).

given constant $C$. The eigenfunctions of a cavity depend on its geometry as well as on possible inhomogeneities (e.g. depth). With other confinements, eigenfunctions may even be more complicated. Nevertheless, they are usually qualitatively similar to trigonometric functions: they oscillate about zero with a characteristic frequency. So we here aim at exploring a variety of functions $\Psi$ that qualitatively represent an eigenfunction. We choose a family of test functions

$$\psi(x,\beta) = \frac{\cos\beta}{\sqrt{\pi}}\sin 3x + \frac{\sin\beta}{\sqrt{\pi}}\sin 5x \qquad (20)$$

These functions are defined orthogonal (and periodic) over $x \in [-\pi/2, 3\pi/2]$, but they can be represented on $x \in [0, \pi/2]$ owing to their symmetry. Varying the shape parameter $\beta \in [0, \pi[$ allows for the exploration of many different configurations of fixed points, as confirmed in figure 2. Seven specific values of $\beta$ have been chosen that

give a comprehensive overview of the different behaviors of $\psi(x,\beta)$.

In the present numerical simulations, the coupling constant $C$ is chosen equal to 0.05, resulting from the following compromise. The average step size $(x_{n+1} - x_n)$ increases with $C$. Consequently, the particle interacts less often with the wave when $C$ is large. It behaves as if it had more inertia. Inertia is a key ingredient for the occurrence of chaos in this model. This can be proven by considering the continuous version where flight times between successive impacts are infinitely short. Position and wave amplitude $[x(t), w(t)]$ are then given by

$$\alpha\ddot{x} + \dot{x} = -Cw\Psi'(x) \text{ and } \dot{w} = -\mu_c w + \Psi(x) \qquad (21)$$

where $\alpha$ is an inertia coefficient and $\mu_c \in [0, \infty[$ the continuous analog of the damping factor $\mu$. When $\alpha = 0$ (no inertia), the system of non-linear ODEs becomes two-dimensional, and therefore cannot exhibit any chaotic behavior. Discretization and inertia somehow play the

same role. Inertia should however be limited, as the particle is not expected to travel more than the cavity size in a single step. The choice $C = 0.05$ is shown to represent a good compromise in terms of inertia, which gives the particle a behavior comparable to the walkers. In the vicinity of the saddles, the position increment $x_{n+1} - x_n$ may be close to the machine epsilon. In order to limit the resulting numerical noise, the map is rewritten as a function of $\tilde{x}_n = x_n - x_b$ as soon as $|\Psi'(x_n)| < 10^{-6}$.

## V. TRANSITION TO CHAOS

Figure 3 shows the evolution of the trajectory with increasing $\mu$ in the $(x, w)$ plane for $\beta = \pi/3$ [16]. At $\mu = 0.8682$ (Fig. 3a), only the rightmost fixed point $x_a$ is still a stable focus about which every trajectory ultimately spirals. This focus experiences a Neimark-Sacker bifurcation at $\mu_a = 0.8795$, so when $\mu = 0.9088$ (Fig. 3b), the focus is unstable and surrounded by a stable limit cycle. In general, the extension of the limit cycles increases with $\mu$, until they collide with the stable manifolds of the saddles in $x = x_b$. For $\beta = \pi/3$, this happens at $\mu \simeq 0.917$. Similarly in (i), the wobbling amplitude is shown to increase with memory until the wobbling orbit collides with the most adjacent unstable orbit [9]. At this stage, a chaotic attractor is revealed as no other stable regular attractor is left (Fig.3c, with $\mu = 0.9369$). The strange attractor has a characteristic multilayered fractal topology. It inflates along $w$ with increasing $\mu$, as shown in Fig.3d for $\mu = 0.9924$. The Lyapunov exponent is positive in the chaotic regime (Figure 4): trajectories initially separated by $\Delta x = 10^{-10}$ (and $\Delta w = 0$) are fully decorrelated after about 170 iterations. This corresponds to the approximate time required to travel once along the chaotic attractor. So a strong dependence to initial conditions is indeed observed in this chaotic regime. A typical chaotic trajectory is shown in Figure 5 [17]. The particle is attracted to the stable manifold of a saddle $x_b$. Then, the wave amplitude $w$ builds up as the particle moves along this manifold. Ultimately, the particle is ejected along the unstable manifold. The direction of ejection is very sensitive to initial conditions. Once ejected, the particle quickly reaches another adjacent saddle.

Transition to chaos is summarized in the bifurcation diagram $(x, \mu)$ of Figure 6(a-b) for $\beta = 0$ and $\beta = \pi/3$. The likelihood (Probability Distribution Function - PDF) to find the particle at a given position $x$ is also represented. In the chaotic regime, peaks of the PDF (resp. troughs) are observed at positions $x_b$ (resp. $x_a$), which simply reflects that the faster a particle moves, the less time it spends about a given location. Figure 6(c-d) represents the PDF for a given value of $\mu > \mu_c$. It shows that in the chaotic regime, the PDF (here calculated over $2 \cdot 10^6$ successive positions from the initial condition $x_0 = 0.1$

and $w_0 = 0.1$) approximately satisfies

$$PDF(x) \simeq \frac{1}{c_0 |\Psi'(x)|} \quad (22)$$

where $c_0$ is a fitting parameter. So in this iterated map (9) aimed at capturing wave-particle coupling, the wave function $\Psi(x)$ directly shapes the PDF of the particle position. A similar behavior has been observed in (iii), where both the radial velocity of the walker and its subsequent PDF are also shaped by the eigenmode of the cavity. There, in the chaotic regime, peaks [resp. troughs] of likelihood are systematically observed in $r_b$ [resp. $r_a$]. It has to be noted that equation (22) is approximative and empirical. The apparent noise in the PDF correspond to higher frequency oscillations that are not removed with either a larger sample of impacts or more bins.

## VI. INTERMITTENT DYNAMICS

A closer look at a chaotic sequence (Fig. 5) confirms that the particle spends most of its time in the immediate vicinity of the stable manifolds $x_b$. It switches from one manifold to the next after a certain time $\tau_b$, different for each $x_b$. The statistical distribution of $\tau_b$ for a large number of successive passages of the same particle is represented in Figure 7(a). Saddles with $\Psi_b \cdot \Psi_b'' < 0$ have a sharp asymmetric distribution from which an average time $< \tau_b >$ can unambiguously be defined. By contrast, as soon as a saddle with $\Psi_b \cdot \Psi_b'' > 0$ is present (here at $\beta = \pi/6$, cf. Fig. 2b), the time distribution is significantly broader and the average is less representative.

Figure 7(b) shows that the ensemble average $< \tau_b >$ over many passages about the saddle point $x_b$ is directly related to its largest eigenvalue:

$$< \tau_b > \simeq \frac{3.5}{C |\Psi_b \Psi_b''|} \quad (23)$$

This relationship has been tested for seven different values of $\beta$ and the corresponding 15 different saddles represented in figure 2. The agreement is excellent, and the proportionality constant only slightly depends on $\mu$. The only points that fail to satisfy this equation are the ones for which the distribution of $\tau_b$ is not a sharp peak (i.e. when there is a saddle for which $\Psi_b \Psi_b'' < 0$). So here again, the wave function $\Psi(x)$ determines the probability to find the particle in the vicinity of saddles $x_b$. One could see these saddles as discrete eigenstates of the system, which probability is weighted by $1/(\Psi_b \Psi_b'')$. Any linear superposition of these eigenstates can be achieved with an appropriate $\Psi(x)$. In the chaotic regime of all configurations (i-iii), the walker trajectory can also be decomposed into segments of regular orbits considered as the eigenstates of the system. The walker stays in each eigenstate for a certain time before it quickly switches to another. In case (iii), these eigenstate orbits are precisely located about $r_b$. In case (i) though, the eigenstates are
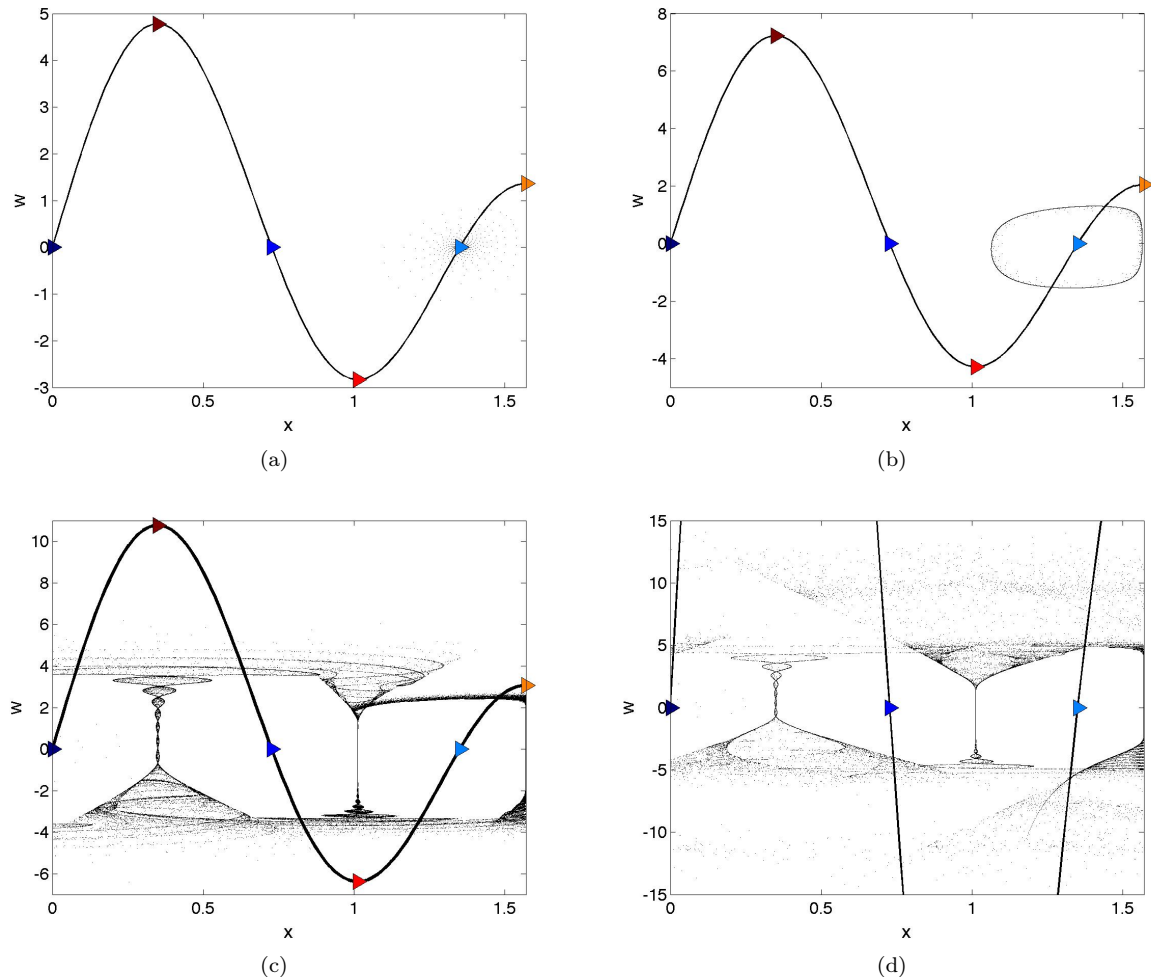
FIG. 3. (Color online) Phase diagrams $(x, w)$ for $\beta = \pi/3$. (a) Stable fixed point (right) at $\mu = 0.8682$. (b) Limit cycle at $\mu = 0.9088$. (c) Strange attractor (early chaos) at $\mu = 0.9369$. (d) Strange attractor (fully-developed chaos) at $\mu = 0.9924$. Blue tone (resp. red tone) symbols represent fixed points $x_a$ (resp. $x_b$). The solid line is the null cline $w = \mu \Psi(x)/(1 - \mu)$.

located in $r_a$ at high memory [15]. This is one of the few qualitative differences between predictions of the simplified map and the radial dynamics in experiments.

The "unfolded" trajectory $x_n$ (considering that $\psi(x, \beta)$ is a periodic function) indicates that the particle switches randomly from one stable manifold to the next, either left or right (Fig.8a). Therefore, the long term behavior of the particle is equivalent to a 1D random walk. The particle diffuses, and the variance of the travelled distance $(x_{n+N} - x_n)$ grows linearly with time $N$, as shown in Fig.8b. The diffusion coefficient $D \simeq 0.019$ can be estimated from the average intermittency time $< \tau_b > \simeq 22$ and the average spacing between saddles $\Delta x_b \simeq 0.63$:

$$D \simeq \frac{(\Delta x_b)^2}{< \tau_b >} \qquad (24)$$

This diffusion coefficient increases linearly with $C$ for $C < 0.08$, which reflects that $< \tau_b > \sim C^{-1}$. The order of magnitude chosen for $C \sim 0.05$ can now be justified.

A close examination at the chaotic trajectory in configuration (iii) [12] reveals that the walker changes direction about every Faraday wavelength. This distance can then be considered as the elementary step of an analog random walk, or the equivalent of $\Delta x_b$ in this model. It is travelled in approximately 17 rebounds in [12], which is of the same order of magnitude as the intermittency time $< \tau_b >$ for $C = 0.05$.

## VII. DISCUSSION

In 1927, Louis de Broglie presented his pilot-wave interpretation of quantum mechanics [18] at the fifth Solvay conference. In this deterministic theory, quantum particles are guided by a pilot wave that satisfies Schrodinger equation. The particles do not exert any instantaneous and individual feedback on the wave. The theory was later extended by Bohm [19]. If the wave is regular,
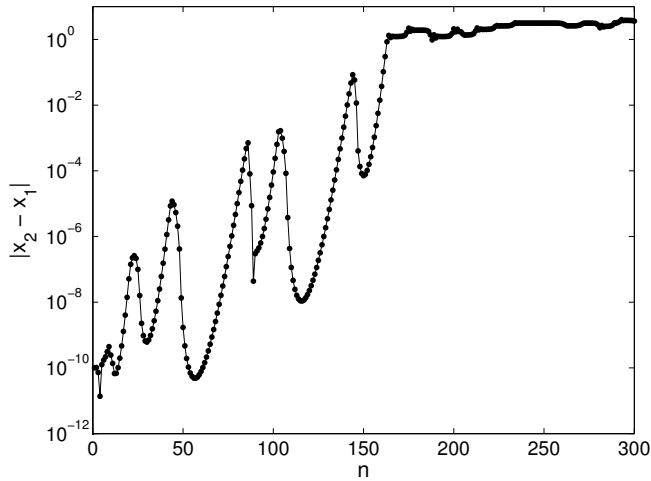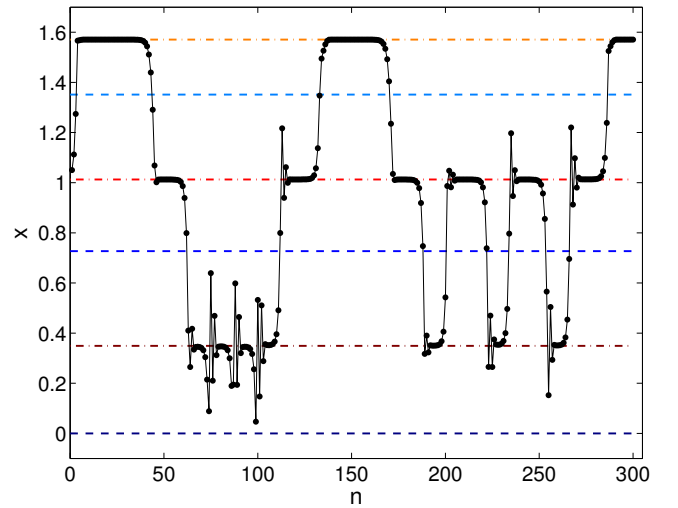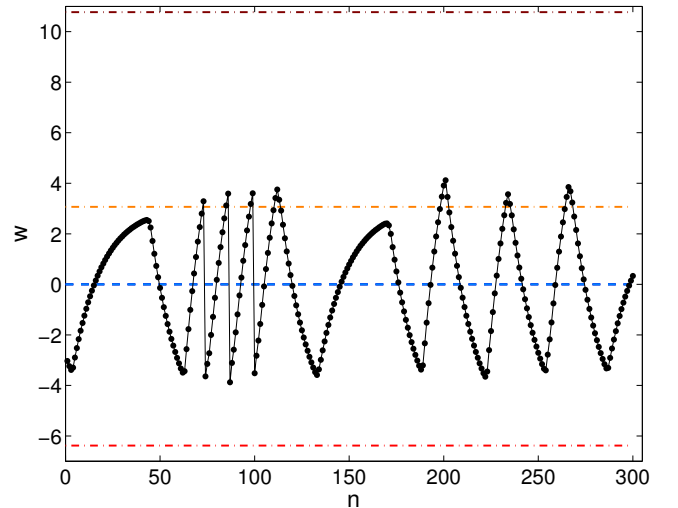
FIG. 4. Diverging distance between two trajectories initially separated by $\Delta x = 10^{-10}$ and $\Delta w = 0$. Parameters are $\beta = \pi/3$ and $\mu = 0.9369$.



(a)



(b)

FIG. 5. (Color online) Trajectory in the chaotic regime ($\beta = \pi/3$, $\mu = 0.9369$). The particle switches intermittently between the different manifolds $x_b$ (red-tone dash-dot lines) and constantly avoids the unstable fixed points (blue-tone dashed lines). The trajectory has been folded on the interval $x \in [0, \pi/2]$, owing to the symmetry and periodicity of $\Psi(x)$.

the particle trajectory predicted by pilot-wave theories is usually regular, although it may become chaotic in some confined geometry [20]. One shortcoming of Bohmian mechanics is that the particle does move only when multiple eigenmodes are considered. Indeed, the particle velocity is proportional to $\psi^* \nabla \psi - \psi \nabla \psi^*$ which amounts to zero for a single cavity mode $\psi(\mathbf{x}, t) = \Psi(\mathbf{x}) e^{-iEt/\hbar}$. The statistical behavior of quantum mechanics is more often explained by the inherently chaotic wave field generated by the presence of a large number of particles [21]. By contrast, the walkers discovered by Couder and co-workers represent a macroscopic wave-particle coupling where the guiding wave originates from the particle itself. When confined, individual walkers experience chaotic trajectories during which they permanently switch between unstable orbits analog to discrete eigenstates. The resulting statistics of walker position reflects the geometry of the wave field.

In this paper, a two-dimensional iterated map (Eq.9) is proposed that models the wave-particle coupling of confined walkers in a mathematically simple way, originating from spectral decomposition. It does not have the shortcoming of Bohmian mechanics, as chaotic motion is produced in any cavity from a single eigenmode. Another model was previously proposed by D. Shirokoff [13] to describe walkers in a square cavity (for which no experiments have been reported yet). There the mathematical description is significantly more complex. The consideration of boundaries was not addressed with spectral decomposition, but rather with the method of mirror images. Unfortunately this method becomes impracticable at high memory, where a prohibitively large number of images resulting from previous impacts has to be considered. Consequently, Shirokoff's model could only be investigated in the low memory regime. Chaos is nevertheless observed when the coupling parameter $F$ (equiv-

alent to $C$ in the present model) is sufficiently large. The PDF of the trajectory at high $F$ also seems to reflect the symmetry of the cavity and the shape of stable orbits at small $F$, although this similarity has not been quantified.

The present map overcomes these shortcomings. When thought as the radial component of the walker trajectory, it captures many features of walker behavior in confined environments. Similarities include (1) the families of regular orbits in the low memory regime; (2) the sequence of destabilization of these trajectories and route to chaos as the memory parameter is increased; (3) the chaotic trajectory being a composition of eigenstates reminiscent of the unstable regular orbits; and (4) the relationship
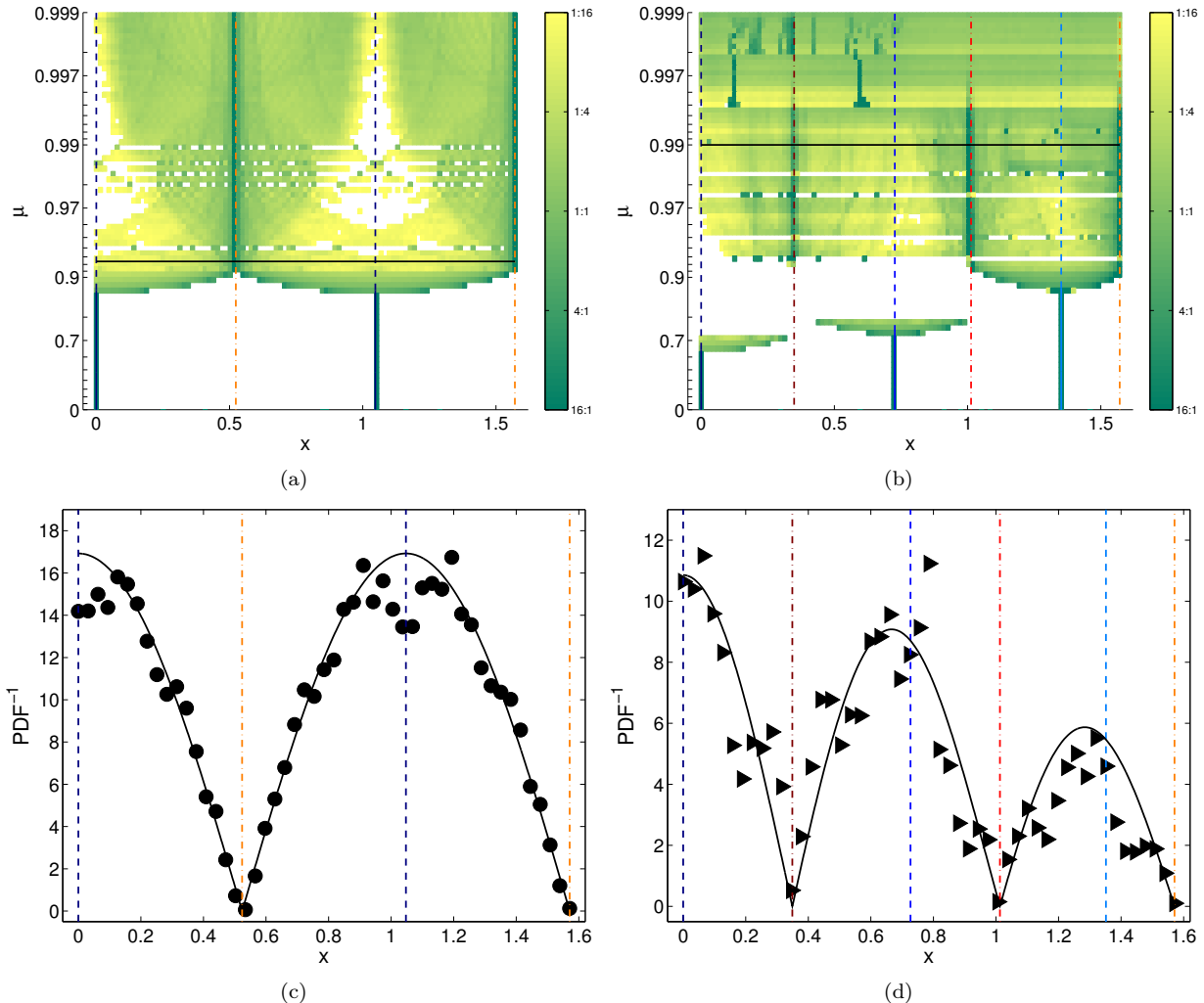
FIG. 6. (Color online) – (a-b) Bifurcation diagram $(x, \mu)$ for $\Psi = \psi(x, \beta)$ for $\beta = 0$ (a) and $\beta = \pi/3$ (b). Yellow to green color (light to dark gray) represents the likelihood to find the particle at a given position $x$, normalized by the probability of a uniform distribution. A position coded $16 : 1$ (resp. $1 : 16$) is 16 times more (resp. less) likely than if the distribution was uniform. Fractions below $1 : 16$ are set to white. The horizontal line indicates the value of $\mu$ selected in (c-d). (c-d) Correlation between the inverse of the Probability Distribution Function (symbols) and $|\Psi'(x)|$. The black solid line corresponds to $c_0|\Psi'(x)|$. Parameters are (c) $\mu = 0.9241$, $c_0 = 10$; and (d) , $\mu = 0.99$, $c_0 = 3.3$. In (a-d), vertical lines correspond to the fixed points. Line style refers to fixed point stability: (solid) stable, (dashed) unstable, (dash-dot) saddle.

between the wave field and the PDF of the walker position. It is shown here that these four properties are almost not dependent on the wave shape $\Psi(x)$. They are also shared by several configurations of confinement in which walkers have been observed. Consequently, they are unaffected by the extreme simplification of the mathematical description proposed herein. Nevertheless, the exact relationship between $\Psi(x)$ and the probability distribution depends on the nature of the coupling between the wave and the particle. Future work could include the search for a wave-particle coupling dynamics that yields

$PDF(x) \sim |\Psi(x)|^2$ as observed in quantum mechanics.
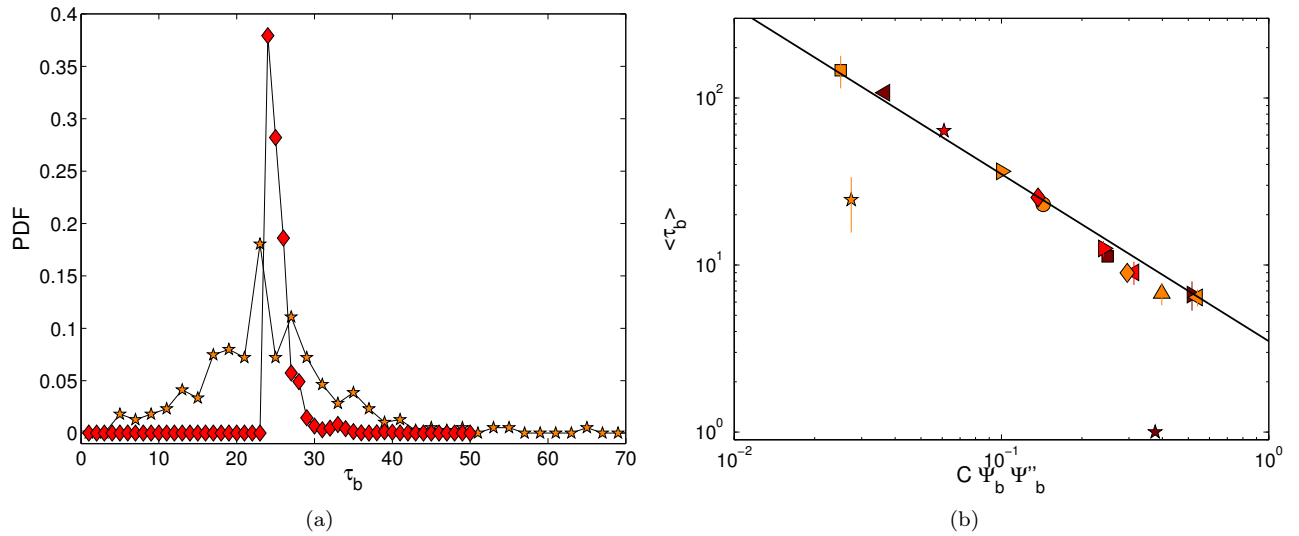
FIG. 7. (Color online) (a) Probability distribution of $\tau_b$ for $\beta = 11\pi/12$ (♦) and $\beta = \pi/6$ (★). (b) Average intermittency time $< \tau_b >$ for $\Psi = \psi(x, \beta)$ with $\mu = 0.997$. Seven different values of $\beta$ are considered; the corresponding symbols and colors are defined in Fig.2. Error bars correspond to the standard deviation of $\tau_b$. The solid line corresponds to Eq. (23).
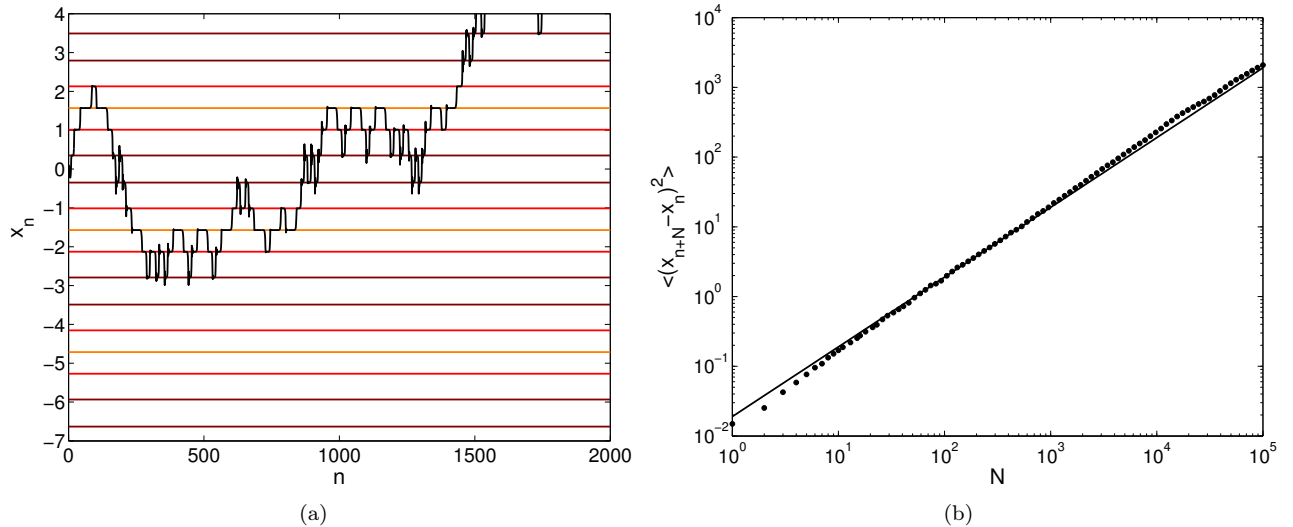


FIG. 8. (Color online) Unfolded chaotic trajectory ($\beta = \pi/3$, $\mu = 0.9369$). (a) The trajectory jumps between saddles in a random way. (b) Evidence of a diffusive behavior in $x$. The solid line corresponds to $< (x_{n+N} - x_n)^2 >= 0.019N$.

[1] A. Eddi, E. Sultan, J. Moukhtar, E. Fort, M. Rossi, and Y. Couder, J. Fluid Mech., **674**, 433 (2011).
[2] J. Molacek and J. W. M. Bush, J. Fluid Mech., **727**, 612 (2013).
[3] A. U. Oza, R. R. Rosales, and J. W. M. Bush, J. Fluid Mech., **737**, 552 (2013), ISSN 1469-7645.
[4] Y. Couder and E. Fort, Phys. Rev. Lett., **97**, 154101 (2006).
[5] A. Eddi, E. Fort, F. Moisy, and Y. Couder, Phys. Rev. Lett., **102**, 240401 (2009).
[6] A. Eddi, J. Moukhtar, S. Perrard, E. Fort, and Y. Couder, Phys. Rev. Lett., **108**, 264503 (2012).
[7] J.W.M. Bush, Annu. Rev. Fluid Mech., **47**, 269 (2015).
[8] E. Fort, A. Eddi, A. Boudaoud, J. Moukhtar, and Y. Couder, PNAS, **107**, 17515 (2010).
[9] D. M. Harris and J. W. M. Bush, J. Fluid Mech., **739**, 444 (2014).
[10] A. U. Oza, D. M. Harris, R. R. Rosales, and J. W. M. Bush, J. Fluid Mech., **744**, 404 (2014).
[11] S. Perrard, M. Labousse, M. Miskin, E. Fort, and Y. Couder, Nature Comm., **5**, 3219 (2014).
[12] D. M. Harris, J. Moukhtar, E. Fort, Y. Couder, and J. W. M. Bush, Phys. Rev. E, **88**, 011001 (R) (2013).
[13] D. Shirokoff, Chaos, **23**, 013115 (2013).

[14] K. Kumar and L. Tuckerman, J. Fluid Mech., **279**, 49 (1994).

[15] A. U. Oza, O. Wind-Willassen, D. M. Harris, R. R. Rosales, and J. W. M. Bush, Phys. Fluids, **26**, 082101 (2014).

[16] See Supplemental Material at [URL] for an animated evolution of the phase diagram with increasing $\mu$.

[17] See Supplemental Material at [URL] for an animated version of this figure.

[18] L. de Broglie, *Ondes et mouvements*, edited by G.-V. et cie (Gauthier-Villars et cie, 1926).

[19] D. Bohm and J.-P. Vigier, Phys. Rev., **96**, 208 (1954).

[20] O. de Alcantara Bonfim, J. Florencio, and F. Sa Barreto, Phys. Rev. E, **58**, R2693 (1998).

[21] P. Gueret and J.-P. Vigier, Foundations of Physics, **12**, 1057 (1982).